

Annihilation of electroweak dumbbells

Teerthal Patel* Tanmay Vachaspati*,†

**Physics Department, Arizona State University, Tempe, Arizona 85287, USA.*

†*Theoretical Physics Department, CERN, 1211 Geneva 23, Switzerland.*

E-mail: tpatel28@asu.edu, tvachasp@asu.edu

ABSTRACT: We study the annihilation of electroweak dumbbells and the dependence of their dynamics on initial dumbbell length and twist. Untwisted dumbbells decay rapidly while maximally twisted dumbbells collapse to form a compact sphaleron-like object, before decaying into radiation. The decay products of a dumbbell include electromagnetic magnetic fields with energy that is a few percent of the initial energy. The magnetic field from the decay of twisted dumbbells carries magnetic helicity with magnitude that depends on the twist, and handedness that depends on the decay pathway.

Contents

1	Introduction	1
2	Model	2
2.1	Initial dumbbell configuration	3
3	Numerical simulation	4
4	Results	6
4.1	Estimating lifetimes	7
4.2	Relic Magnetic Fields	8
5	Discussion and Conclusion	11
A	Semilocal Dumbbell simulations	14

1 Introduction

The “electroweak dumbbell” consists of a magnetic monopole and an antimonopole of the standard electroweak model connected by a string made of Z magnetic field [1, 2]. The existence of such non-perturbative field configurations in the electroweak model is of great interest as they can provide the first evidence for (confined) magnetic monopoles. In a cosmological context, dumbbells can source large-scale magnetic fields which can seed galactic magnetic fields and play an important role in the propagation of cosmic rays [3].

Electroweak dumbbells are often regarded as magnetic dipoles, with the magnetic field strength falling off as $1/r^3$ with the distance r from the dipole. However the situation is richer: there is a one-parameter set of electroweak dumbbell configurations [4], all describing a confined monopole-antimonopole pair, but with additional structure called the “twist”. In our previous work [5], we have shown that the magnetic field strength of the maximally twisted dumbbell falls off asymptotically as $\cos\theta/r^2$ (in spherical coordinates), a gross departure from the usual dipolar magnetic field. The twisted dumbbell configuration was proposed in [4] and is closely related to the electroweak sphaleron [6–9].

The dynamics of electroweak sphalerons and dumbbells are of particular interest in the efforts towards detecting them in experiments. In view of ongoing experiments like the Monopole and Exotics Detector (MoEDAL) at the Large Hadron Collider (LHC) [10], Ref. [11] recently studied the production of the electroweak sphaleron in the presence of strong magnetic fields that arise during heavy ion collisions. In the cosmological context, simulations of the dynamical decay of electroweak sphalerons have been conducted to study baryogenesis and magnetogenesis [12, 13]. Thus, there have been several efforts to numerically resolve the configuration and dynamics of electroweak sphalerons. The relevance of

dynamics of electroweak dumbbells was first alluded to by Nambu [1] wherein he showed that electroweak dumbbells could be stabilized by rotation, potentially making them long lived enough to have significant implications in experimental searches. This, along with a lack of detailed study of the dynamics of electroweak dumbbells, has motivated our investigation into the dumbbell configurations and their dynamics.

In this article, we investigate the dynamical evolution of an initially stationary dumbbell configuration for a range of twists and initial dumbbell lengths. The initial condition is found by numerically relaxing a “guess” dumbbell configuration under the constraint that locations of the monopole and antimonopole remain fixed, according to the method outlined in our previous work [5]. The main quantities of interest that we analyze are the dumbbell lifetimes and the magnetic field produced during the decay. The untwisted dumbbells are found to be unstable, with the monopoles immediately undergoing annihilation as expected. Twisted dumbbells, on the other hand, lead to the creation of an intermediate sphaleron configuration after the initial collapse, and subsequently decay into helical magnetic fields with relatively stronger field strength.

The article begins with a description of the model and our initial configuration in Section 2. The numerical simulation setup is described in Section 3. Our results for the lifetimes and the relic magnetic fields are given in Section 4, and we discuss our conclusions in Section 5.

2 Model

The Lagrangian for the bosonic sector of the electroweak theory is given by

$$\mathcal{L} = -\frac{1}{4}W_{\mu\nu}^a W^{a\mu\nu} - \frac{1}{4}Y_{\mu\nu} Y^{\mu\nu} + |D_\mu\Phi|^2 - \lambda(|\Phi|^2 - \eta^2)^2, \quad (2.1)$$

where

$$D_\mu \equiv \partial_\mu - \frac{i}{2}g\sigma^a W_\mu^a - \frac{i}{2}g'Y_\mu. \quad (2.2)$$

Here, Φ is the Higgs doublet, W_μ^a are the SU(2)-valued gauge fields with $a = 1, 2, 3$ and, Y_μ is the U(1) hypercharge gauge field. In addition, σ^a are the Pauli spin matrices with $\text{Tr}(\sigma^a\sigma^b) = 2\delta_{ab}$, and the experimentally measured values of the parameters that we adopt from [14] are $g = 0.65$, $\sin^2\theta_w = 0.22$, $g' = g \tan\theta_w = 0.35$, $\lambda = 0.129$ and $\eta = 174$ GeV.

The classical Euler-Lagrange equations of motion for the model are given by

$$D_\mu D^\mu\Phi + 2\lambda(|\Phi|^2 - \eta^2)\Phi = 0 \quad (2.3)$$

$$\partial_\mu Y^{\mu\nu} = g' \text{Im}[\Phi^\dagger(D^\nu\Phi)] \quad (2.4)$$

$$\partial_\mu W^{a\mu\nu} + g\epsilon^{abc}W_\mu^b W^{c\mu\nu} = g \text{Im}[\Phi^\dagger\sigma^a(D^\nu\Phi)] \quad (2.5)$$

where the gauge field strengths are given by

$$W_{\mu\nu}^a = \partial_\mu W_\nu^a - \partial_\nu W_\mu^a + g\epsilon^{abc}W_\mu^b W_\nu^c \quad (2.6)$$

$$Y_{\mu\nu} = \partial_\mu Y_\nu - \partial_\nu Y_\mu. \quad (2.7)$$

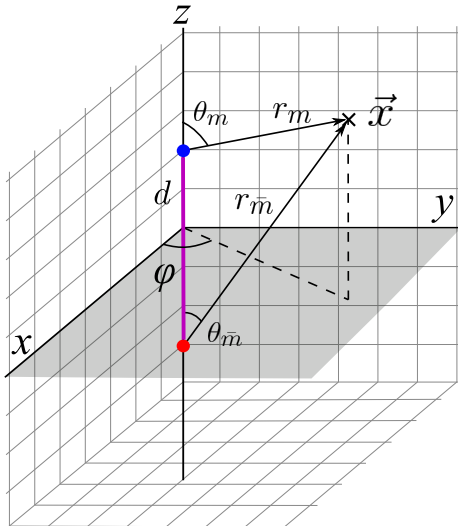


Figure 1: The location of the monopole (blue dot), antimonopole (red dot) and the Z -string (purple line) in a cartesian grid.

Electroweak symmetry breaking results in three massive gauge fields, namely the two charged W^\pm bosons and Z_μ , and one massless gauge field, A_μ , that is the electromagnetic gauge field. We define

$$Z_\mu \equiv \cos \theta_w n^a W_\mu^a + \sin \theta_w Y_\mu, \quad (2.8)$$

$$A_\mu \equiv -\sin \theta_w n^a W_\mu^a + \cos \theta_w Y_\mu, \quad (2.9)$$

where

$$n^a \equiv \frac{\Phi^\dagger \sigma^a \Phi}{|\Phi|^2} \quad (2.10)$$

are components of a unit three vector \hat{n} . The weak mixing angle, θ_w is given by $\tan \theta_w = g'/g$, the Z coupling is defined as $g_Z \equiv \sqrt{g^2 + g'^2}$, and the electric charge is given by $e = g_Z \sin \theta_w \cos \theta_w$. The Higgs, Z and W boson masses are given by $m_H \equiv 2\sqrt{\lambda}\eta = 125$ GeV, $m_Z \equiv g_Z \eta / \sqrt{2} = 91$ GeV and $m_W \equiv g\eta / \sqrt{2} = 80$ GeV, respectively.

2.1 Initial dumbbell configuration

We construct a suitable initial configuration for dumbbell dynamics by first choosing a “guess” field configuration that contains a monopole and antimonopole separated by a distance $2d$ and with relative twist γ [2]. In the asymptotic region,

$$\hat{\Phi}_{m\bar{m}}(\gamma) = \begin{pmatrix} \sin(\theta_m/2) \sin(\theta_{\bar{m}}/2) e^{i\gamma} + \cos(\theta_m/2) \cos(\theta_{\bar{m}}/2) \\ \sin(\theta_m/2) \cos(\theta_{\bar{m}}/2) e^{i\phi} - \cos(\theta_m/2) \sin(\theta_{\bar{m}}/2) e^{i(\phi-\gamma)} \end{pmatrix}. \quad (2.11)$$

The monopole and antimonopole are located along the z -axis at $z = \pm d$, with θ_m and $\theta_{\bar{m}}$ being the spherical polar angles as measured from the monopole and antimonopole, respectively; ϕ is the azimuthal angle. The coordinate system is illustrated in Figure 1. In the limit $\theta_{\bar{m}} \rightarrow 0$, (2.11) reduces to the monopole configuration, and in the limit $\theta_m \rightarrow 0$ to

an antimonopole. In between the monopole and antimonopole, $\theta_m \rightarrow \pi$ and $\theta_{\bar{m}} \rightarrow 0$, the configuration is that of a Z -string.

The asymptotic gauge field configurations are obtained by setting the covariant derivative of the Higgs field to vanish,

$$gW_\mu^a = -\epsilon^{abc}n^b\partial_\mu n^c + i\cos^2\theta_w n^a(\Phi^\dagger\partial_\mu\Phi - \partial_\mu\Phi^\dagger\Phi) \quad (2.12)$$

$$g'Y_\mu = -i\sin^2\theta_w(\Phi^\dagger\partial_\mu\Phi - \partial_\mu\Phi^\dagger\Phi) \quad (2.13)$$

To correctly account for the spatial dependence of the Higgs field around the monopole-antimonopole pair, we attach spatial profiles. Including this in the ansatz, the initial monopole-antimonopole scalar field configuration is given by

$$\Phi_{m\bar{m}} = k(\vec{r})h(r_m)h(r_{\bar{m}})\hat{\Phi}_{m\bar{m}}, \quad (2.14)$$

where r_m and $r_{\bar{m}}$ are the radial coordinates centered on the monopole and antimonopole, respectively, given by

$$r_m = |\mathbf{x} - \mathbf{x}_m|, \quad r_{\bar{m}} = |\mathbf{x} - \mathbf{x}_{\bar{m}}|. \quad (2.15)$$

The function $k(\vec{r})$ is the Z -string profile. Similar to the Higgs, we include spatial profiles for the gauge fields as

$$gW_\mu^a = l(\vec{r})j(r_m)j(r_{\bar{m}})[- \epsilon^{abc}n^b\partial_\mu n^c + i\cos^2\theta_w n^a(\hat{\Phi}^\dagger\partial_\mu\hat{\Phi} - \partial_\mu\hat{\Phi}^\dagger\hat{\Phi})] \quad (2.16)$$

$$g'Y_\mu = l(\vec{r})j(r_m)j(r_{\bar{m}})[-i\sin^2\theta_w(\hat{\Phi}^\dagger\partial_\mu\hat{\Phi} - \partial_\mu\hat{\Phi}^\dagger\hat{\Phi})] \quad (2.17)$$

We have previously used numerical relaxation to solve for the Higgs and gauge field profile of a static dumbbell in with the constraint that the topology of the monopole and antimonopole remain fixed during the relaxation process [5]. We use the same procedure to find the initial field configurations that we will then evolve to study dumbbell dynamics.

3 Numerical simulation

We have used a numerical relativity technique adapted from [15], and previously used in [16] to study monopole-antimonopole scattering in the $SO(3)$ model. Adopting the temporal gauge for convenience in numerical implementation, $W_0^a = Y_0 = 0$, the evolution equations (2.3)-(2.5) can be written as

$$\partial_0^2\Phi = D_i D_i \Phi - 2\lambda(|\Phi|^2 - \eta^2)\Phi \quad (3.1)$$

$$\partial_0^2 Y_i = -\partial_j Y_{ij} + g' \text{Im}[\Phi^\dagger(D_i\Phi)] \quad (3.2)$$

$$\partial_0^2 W_i^a = -\partial_j W_{ij}^a - g\epsilon^{abc}W_j^b W_{ij}^c + g \text{Im}[\Phi^\dagger\sigma^a(D_i\Phi)]. \quad (3.3)$$

Straightforward discretization of the evolution equations leads to numerical instabilities. To control the instabilities, we introduce ‘‘Gauss constraint variables’’ $\Xi = \partial_i Y_i$ and $\Gamma^a = \partial_i W_i^a$, with their respective evolution equations

$$\partial_0\Xi = \partial_0 Y_{0i} - g_p^2\{\partial_0 Y_{0i} - g' \text{Im}[\Phi^\dagger(\partial_0\Phi)]\} \quad (3.4)$$

$$\partial_0\Gamma^a = \partial_0 W_{0i}^a - g_p^2\{\partial_0 W_{0i}^a + g\epsilon^{abc}W_i^b\partial_0 W_i^c - g \text{Im}[\Phi^\dagger\sigma^a(\partial_0\Phi)]\}. \quad (3.5)$$

Here, we have introduced the numerical stability parameter g_p^2 . These equations reduce to the Gauss constraints in the continuum, regardless of the choice of g_p^2 . However, once the system of equations is discretized for numerical evolution, the term in the curly brackets do not always vanish, and a non-zero value of g_p^2 ensures numerical stability as outlined in [15]. The equations in (3.1)-(3.3) are now written with the Gauss constraint variables as

$$\begin{aligned} \partial_0^2 \Phi &= \nabla^2 \Phi - i \frac{g}{2} \sigma^a W_i^a \partial_i \Phi - i \frac{g'}{2} Y_i \partial_i \Phi - i \frac{g}{2} \sigma^a \Gamma^a \Phi - i \frac{g'}{2} \Xi \Phi \\ &\quad - i \frac{g}{2} \sigma^a W_i^a (D_i \Phi) - i \frac{g'}{2} Y_i (D_i \Phi) - 2\lambda(|\Phi|^2 - \eta^2)^2 \Phi \end{aligned} \quad (3.6)$$

$$\partial_0^2 Y_i = \nabla^2 Y_i - \partial_i \Xi + g' \text{Im}[\Phi^\dagger \sigma^a (D_i \Phi)] \quad (3.7)$$

$$\begin{aligned} \partial_0^2 W_i^a &= \nabla^2 W_i^a + \partial_i \Gamma^a - g \epsilon^{abc} (\partial_k W_i^b) W_k^c - g \epsilon^{abc} W_i^b \Gamma^c \\ &\quad - g \epsilon^{abc} W_k^b W_{ik}^c + g \text{Im}[\Phi^\dagger \sigma^a (D_i \Phi)] \end{aligned} \quad (3.8)$$

Our simulations are conducted on a regular cubic lattice with Dirichlet boundary conditions and the fields are evolved in time using the explicit Crank-Nicholson method with two iterations [17]. We adopted phenomenological values for the electroweak model as given in Sec. 2. We choose to work in units of η and set its numerical value to $\eta = 1$ in our simulations. Then the Higgs mass of 125 GeV in these units is given by $2\eta\sqrt{\lambda} = 2\sqrt{\lambda} = 0.72$. Similarly, the W boson mass is $m_W = g\eta/\sqrt{2} = 0.46$. For most of our runs, we use a lattice of size 400^3 with lattice spacing $\delta = 0.25\eta^{-1} = 0.25$, and time step $dt = \delta/8$. The Compton radius of the W boson is $m_W^{-1} = 2.17$. This is also approximately the radius of the monopole and string in the dumbbell, implying that their profiles have a resolution of roughly 10 grid points in our setup.

The Higgs field vanishes at the centers of the monopole, antimonopole and Z -string. Since the initial dumbbell profile involves delicate cancellation of zeros on the dumbbell, we offset the dumbbell location away from the z -axis by half a lattice spacing. That is, the monopole and antimonopole are at the coordinates $x = y = \delta/2, z = \pm(d + \delta/2)$, while the Z -string is located at $x = y = \delta/2$ and parallel to the z -axis.

To ensure that the Dirichlet boundary conditions do not significantly affect the dynamics of the annihilating dumbbell, we only consider initial dumbbell lengths $2d$ that are sufficiently smaller than the lattice size. The maximum separation considered in our simulations was slightly less than half the lattice width and we ensure that the Higgs field is close to the vacuum expectation value near the boundaries $|\Phi| \approx 1$. We run our simulations for $\sim (5 - 10) \times T_c$, where T_c is the dumbbell lifetime, to study the relic energies in the different fields. We ensure that there are no significant effects on the dumbbell dynamics due to reflections from the Dirichlet boundary conditions in the time span considered here. We have tested this by varying the lattice spacing δ and the total simulation box size. Thus we ensure that our choice of numerical parameters and boundary conditions do not affect the dumbbell dynamics.

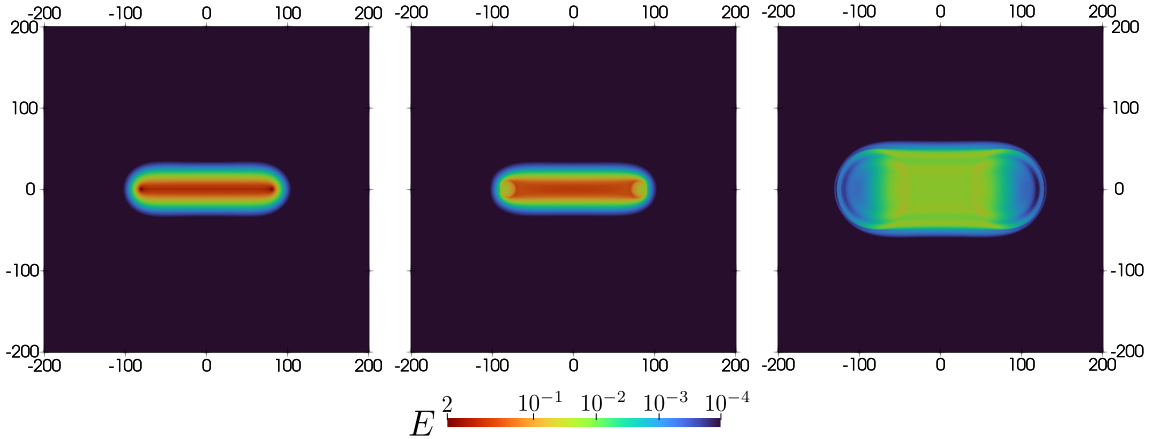


Figure 2: The snapshots of energy density in xz -plane for $\gamma = 0$ are shown for times $0dt$, $1000dt$ and $5000dt$ in the left, middle and right panels, respectively. The colors represent the energy density and the corresponding values are given by the scale, in units of η^4 . Here, the simulation parameters are $dt = \delta/100$, with $\delta = 0.25\eta^{-1}$, and the initial dumbbell length is $2d = 160\delta$. The horizontal (z) and vertical (x) axis are in lattice units.

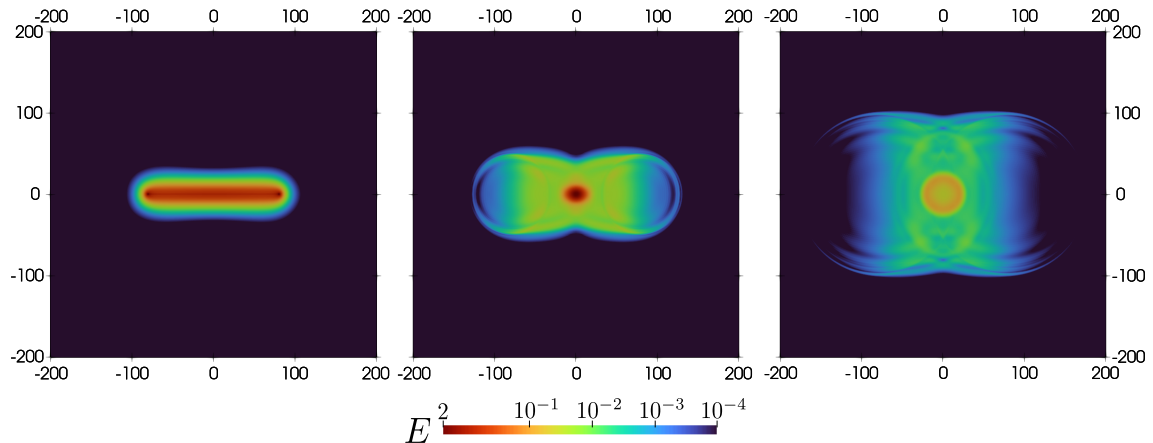


Figure 3: The energy density snapshots, similar to Figure 2, for the twisted case ($\gamma = \pi$) and times $0dt$, $5000dt$ and $10000dt$ in the left, middle and right panels, respectively.

4 Results

We ran the simulation for a range of initial dumbbell lengths and twists. We show several snapshots of the energy density in the xz -plane for the untwisted case ($\gamma = 0$) in Figure 2, and for the twisted case ($\gamma = \pi$) in Figure 3. As can be inferred from these slices, the untwisted dumbbell promptly undergoes annihilation. However, the twisted dumbbell forms an intermediate object that appears as an over-density in the center, before eventually decaying away. We will discuss the relevance of this object (most likely the electroweak sphaleron, as discussed in Ref. [4]) in the context of the dumbbell lifetimes and the relic magnetic energies in the following sections.

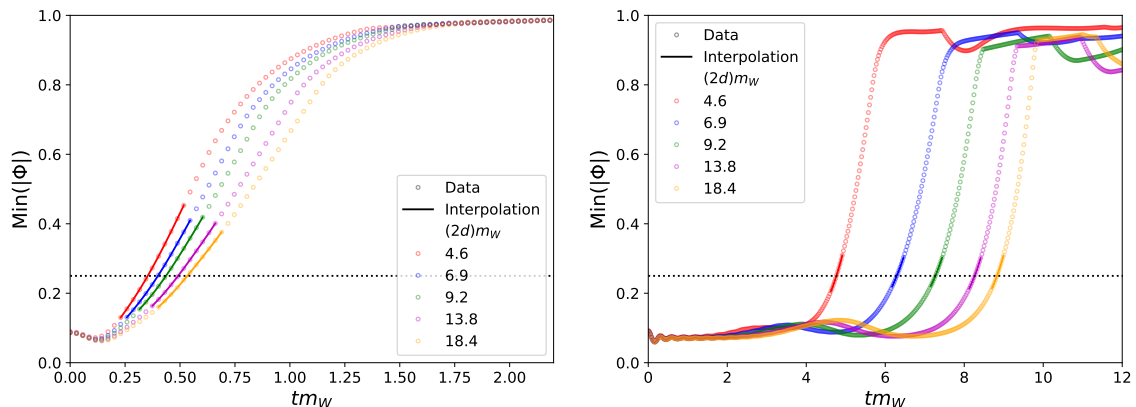


Figure 4: The evolution of $\text{Min}[|\Phi|]$ in the simulation box for twists $\gamma = 0$ (left panel) and π (right panel). The line colors correspond to different values of dumbbell lengths expressed as a multiple of the approximate monopole width m_W^{-1} . The hollow circles correspond to the data points from the simulation and the solid curves are 4th order polynomial fits around the threshold $\text{Min}[|\Phi|] = 0.25$. We show our threshold choice, $\text{Min}[|\Phi|] = 0.25$, as a dotted horizontal line.

4.1 Estimating lifetimes

The magnetic monopoles are zeros in the Higgs field and we leverage this to estimate the lifetime of the dumbbell by tracking the zeros and finding when they disappear in the simulation box. Since the dumbbell is offset by $\delta/2$ in the positive x and y directions in our setup, the zeros of the Higgs field are never located at lattice points. We instead borrow the approach from [16] used in studying the creation of monopoles via classical scattering. We track the evolution of the minimum value of the Higgs field over the entire lattice, $\text{Min}[|\Phi|]$. Once $\text{Min}[|\Phi|]$ exceeds a threshold, we tag the timestep in our simulation as the dumbbell lifetime. The lifetime obtained by this criterion depends on the chosen value of the threshold. As we will see, the result is sensitive to the threshold in the untwisted case but is quite insensitive in the twisted case. Additionally, we have tested the dependence of lifetimes on the spatial and time resolution of the simulation and demonstrated that there were no significant dependencies on the choice of our simulation parameters.

In Figure 4, we show the evolution of $\text{Min}[|\Phi|]$ for various values of initial separation $2d$. Comparing the untwisted (left panel) and twisted (right panel) cases, respectively, we see that the curves for the untwisted case rise slowly, implying greater sensitivity of the dumbbell lifetime to the chosen threshold. In the twisted case, the curves rise very sharply and the dumbbell lifetime is not sensitive to our choice of threshold. After tagging the timestep when the threshold condition on $\text{Min}[|\Phi|]$ is satisfied in our simulations, we interpolate the time evolution of $\text{Min}[|\Phi|]$ in a small range around the tagged timestep. The interpolation was performed via a fourth order polynomial curve fit, and we evaluate the interpolated function at the threshold value ($\text{Min}[|\Phi|] = 0.25$) to find the lifetime. The interpolated $\text{Min}[|\Phi|]$ are shown in Figure 4 as solid lines.

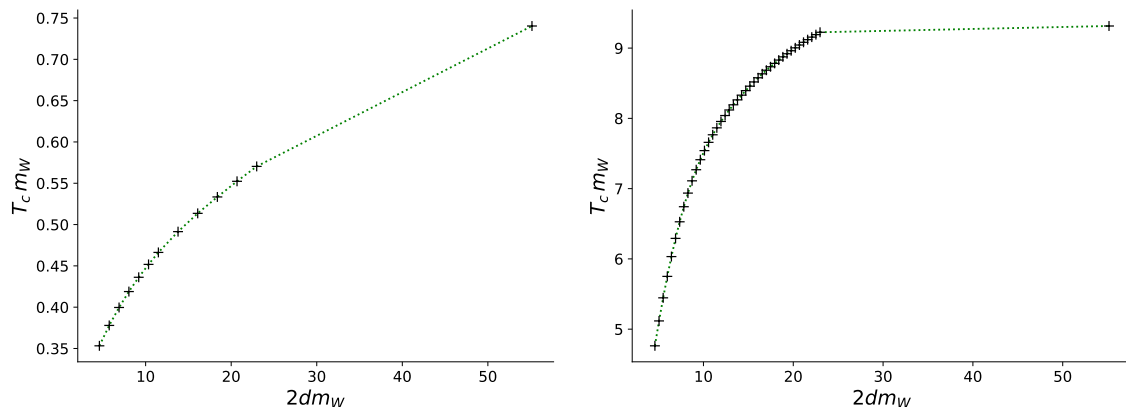


Figure 5: The lifetimes T_c of the dumbbells as a function of their initial separation are shown for twists $\gamma = 0$ and π in the left and right panels, respectively.

We plot the dumbbell lifetime against the initial dumbbell length for untwisted and maximally twisted dumbbells in Figure 5. We find that the lifetime grows with initial length but appears to saturate beyond a certain length. To check the saturation we have performed one run for very long dumbbells ($2dm_W = 55.2$). These runs are computationally very expensive. The saturation is clearer in the case of twisted dumbbells. We interpret these plots recalling the instability analysis of Z-strings [18, 19]: the untwisted dumbbell decays on a timescale $\sim m_W^{-1}$ due to the instability, while the twisted dumbbell survives about 10 times longer, first collapsing to an electroweak sphaleron that eventually decays due to its instability on a longer timescale. To verify that the instability is dynamical and not a result of numerical artifacts, we followed [2, 20] and ran test simulations with large values of $\sin^2 \theta_w$ and small values of m_H/m_Z for which Z-strings are known to be stable [18, 19]. The results of these simulations are given in Appendix A. In contrast to the simulations with physical parameters, the Z-string instability is absent and the dynamics of the monopoles is clearly visible in these “semilocal” simulations.

4.2 Relic Magnetic Fields

The definition for the electromagnetic field strength tensor in the symmetry broken phase ($|\Phi| = \eta$) that reduces to the usual Maxwell definition in unitary gauge is [21, 22],

$$\begin{aligned}
 A_{\mu\nu} &\equiv -\sin \theta_w n^a W_{\mu\nu}^a + \cos \theta_w Y_{\mu\nu} - i \frac{2 \sin \theta_w}{g\eta^2} (D_\mu \Phi^\dagger D_\nu \Phi - D_\nu \Phi^\dagger D_\mu \Phi) \\
 &= \partial_\mu A_\nu - \partial_\nu A_\mu - i \frac{2 \sin \theta_w}{g\eta^2} (\partial_\mu \Phi^\dagger \partial_\nu \Phi - \partial_\nu \Phi^\dagger \partial_\mu \Phi).
 \end{aligned}
 \tag{4.1}$$

This definition implies the presence of non-zero electromagnetic fields even for $A_\mu = 0$ due to the Higgs gradient term. In our study of the decay of dumbbells, $\partial_\mu \Phi$ vanishes at late times and then the expression in (4.1) agrees with the Maxwell definition.

The total magnetic field energy is given by

$$E_M(t) = \frac{1}{2} \int d^3x B^2.
 \tag{4.2}$$

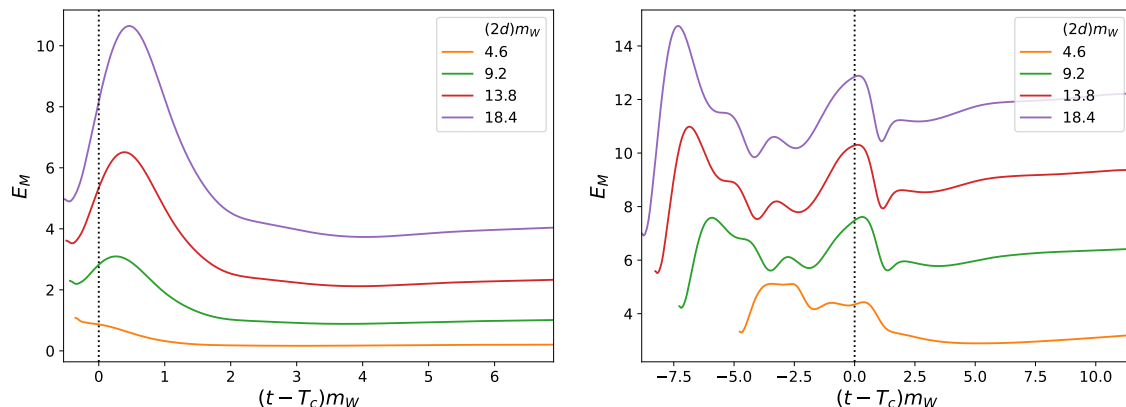


Figure 6: The total magnetic energy as a function of time for twists $\gamma = 0$ and π in the left and right panels, respectively. The time along the horizontal axis is shifted by the lifetime T_c and $t = T_c$ is shown by a vertical dotted line. Different colored curves correspond to different initial dumbbell lengths, as stated in the legends.

We show the time evolution of magnetic energy $E_M(t)$ for twisted and untwisted dumbbells of various initial lengths in Figure 6. After an initial phase of annihilation, the total magnetic field energy reaches a steady value that depends on the initial length of the dumbbell. An important observation is that the relic magnetic energy depends on the twist, in addition to the initial dumbbell lengths. In Figure 7 we plot the fractional magnetic field energy at a late time after annihilation $T_c + \Delta t$, where we have chosen $\Delta t = 25\eta^{-1}$. Since we use Dirichlet boundary conditions, the simulation time has an upper bound, after which reflections occurring at the boundaries would affect quantities of interest. The time at which we evaluate the relic magnetic field energy, $T_c + \Delta t$ is large enough such that the relic magnetic energy has reached an asymptote but is still smaller than the time at which a significant fraction of the energy is reflected. From Figure 7, we infer the fractional magnetic energy, after annihilation, is about twice as large for the twisted case when compared to the untwisted case, for the same initial (large) dumbbell length.

In addition to the magnetic energy density, we are interested in the helicity of the magnetic field, which has been shown to have significant implications for cosmic baryogenesis and magnetogenesis [3, 4, 23]. The total magnetic helicity is defined as

$$H_M(t) = \int d^3x \mathbf{A} \cdot \mathbf{B}, \quad (4.3)$$

where \mathbf{A} is given by the spatial components of the vector potential (2.9) and \mathbf{B} is derived from the EM tensor (4.1).

The evolution of total magnetic helicity for an initially twisted dumbbell is shown by the blue curve in the left panel of Figure 8. It is clear that the helicity does not approach a specific value within the span of our simulation. A possible explanation for the behavior is that the definition of H_M is gauge independent only if the magnetic field is orthogonal to the areal vectors everywhere on the boundaries of the simulation domain. (Alternately, if

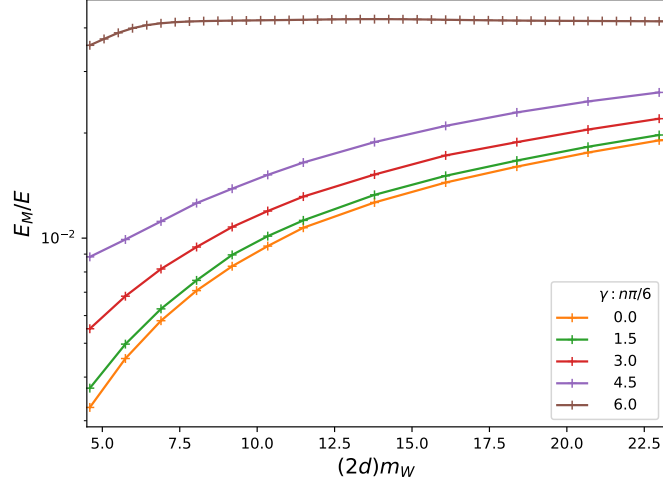


Figure 7: The magnetic energy at a late time, $E_M(T_c+25)$, as a function of initial dumbbell length. The different colors correspond to different values of twists γ as stated in the legend.

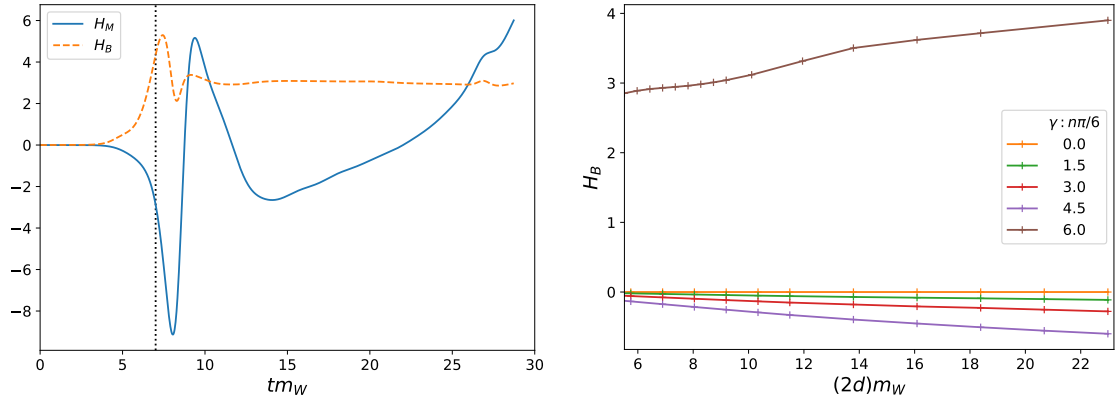


Figure 8: In the left panel, the magnetic helicity $H_M(t)$ (blue curve), and the physical helicity $H_B(t)$ (orange dashed curve) are shown for the twisted case $\gamma = \pi$, with initial dumbbell length $2d = 80\delta$. Here, the annihilation time T_c is marked with a black dotted vertical line. In the right panel, we plot the physical helicity at late time, $H_B(T_c + 25\eta^{-1})$, as a function of the initial dumbbell length, with different colors corresponding to the twist values shown in the legend.

the magnetic field vanishes on the boundaries.) This is certainly not true in our simulations. Hence we cannot assign physical meaning to our evaluation of H_M at late times when the magnetic field is not small at the boundaries. Nonetheless, we can infer that the relic magnetic field has significant net helicity when compared to the untwisted case, which had a helicity $H \sim 10^{-13}$, consistent with numerical roundoff.

An alternative measure of the parity violation in the magnetic field is provided by the “physical helicity” defined as,

$$H_B = \int d^3x \mathbf{B} \cdot (\nabla \times \mathbf{B}). \quad (4.4)$$

In contrast to the magnetic helicity, the physical helicity does not have issues with gauge invariance. It is also better behaved in a finite domain as the magnetic field \mathbf{B} falls off faster than the gauge field \mathbf{A} . The evolution of H_B is shown in Figure 8 for $\gamma = \pi$, and it asymptotes to a constant value at late times. We also plot H_B at late times after annihilation for various initial dumbbell lengths and twists in the right panel of Figure 8. From this, we can infer that the H_B for the untwisted case $\gamma = 0$ is consistent with zero. In the twisted case with $\gamma = \pi$, it takes on finite positive values, $\sim 3\eta^2$, as shown in Figure 8. One feature, that is immediately clear, is that the signs of the physical helicities, H_B , for $\gamma = \pi$ and $0 < \gamma < \pi$ are opposite to each other. The opposite signs are related to the untwisting dynamics of the dumbbell configuration as it annihilates. Dumbbells with twist $\gamma = \pi$ are maximally twisted and carry maximal energy as a function of twist [5]. Dumbbells with twist slightly less than π will tend to untwist by reducing the twist angle from $\pi- \rightarrow 0$, while those with twist somewhat greater than π will untwist by increasing the twist angle from $\pi+ \rightarrow 2\pi$. These decay modes lead to magnetic field helicity of opposite signs. We tested this argument by running the simulation for twists slightly larger and smaller than π , and confirmed that the signs of the physical helicity are indeed opposite to each other. The plots for the tests we conducted, for two different initial dumbbell lengths, are shown in Figure 9, where we see that the evolution of H_B for twist $\pi+$ mirrors the one for twist $\pi-$.

5 Discussion and Conclusion

We have studied the collapse, annihilation, and decay products of electroweak dumbbells as a function of their length and twist.

The untwisted case has the expected dynamics, where the dumbbell collapses in a time that is very short, $\sim m_W^{-1}$, and comparable to the instability time scale of the Z-string [18, 19]. The energy of the dumbbell that is converted into magnetic field energy depends on the length of the dumbbell. For short untwisted dumbbells, the magnetic field energy can be $\sim 0.1\%$; for longer dumbbells it is $\sim 1\%$. The magnetic fields produced in the untwisted case are not helical.

Twisted dumbbells collapse on a time-scale that saturates to $\sim 10m_W^{-1}$ for long dumbbells. They collapse to form a long-lived object that presumably is an electroweak sphaleron, see Figure 3. Eventually, the sphaleron decays as well. The decay products include magnetic

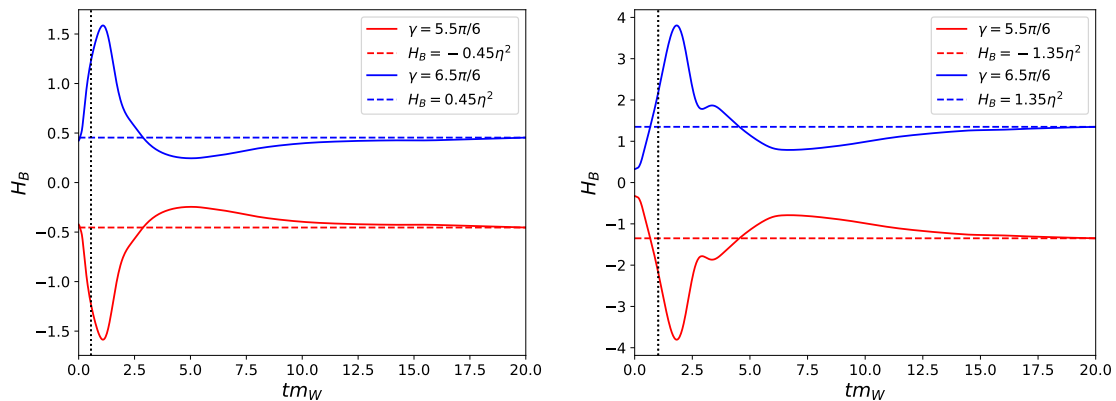


Figure 9: The evolution of physical helicity H_B for twists $\gamma = 5.5\pi/6$ (red curve) and $6.5\pi/6$ (blue curve) are shown for initial dumbbell lengths $2d = 80\delta$ and 160δ in the left and right panels, respectively. The annihilation time T_c is marked with a black dotted vertical line. The horizontal red and blue curves correspond to the physical helicities at time $t = 20m_W^{-1}$. Here, the time step size in the simulation is $dt = \delta/8$, with $\delta = 0.25\eta^{-1}$.

field energy that is large compared to the untwisted case. The fractional energy converted to magnetic field energy is roughly independent of the dumbbell length and is $\sim 4\%$. The produced magnetic field is helical though our calculation of the magnetic helicity is not reliable, especially at late times, due to the finiteness of the simulation box. As an alternative we have calculated the integrated physical helicity and this asymptotes to a constant ($\sim 3\eta^2$), at late times for the maximally twisted dumbbell.

In future work, we propose to study the dynamics of rotating dumbbells as this pertains to their production and detection in a laboratory setting as first discussed by Nambu [1]. We expect the study to be technically challenging as it would require significant improvements in implementing boundary conditions, especially if rotating dumbbells survive for a long time.

Acknowledgments

This work was supported by the U.S. Department of Energy, Office of High Energy Physics, under Award No. DE-SC0019470. The authors acknowledge Research Computing at Arizona State University for providing access to high performance computing and storage resources on the Sol Supercomputer that have contributed to the research results reported within this paper.

References

- [1] Y. Nambu, *String-Like Configurations in the Weinberg-Salam Theory*, *Nucl. Phys. B* **130** (1977) 505.
- [2] A. Achúcarro and T. Vachaspati, *Semilocal and electroweak strings*, *Phys. Rept.* **327** (2000) 347 [[hep-ph/9904229](#)].

- [3] T. Vachaspati, *Progress on cosmological magnetic fields*, *Rept. Prog. Phys.* **84** (2021) 074901 [[2010.10525](#)].
- [4] T. Vachaspati and G.B. Field, *Electroweak string configurations with baryon number*, *Phys. Rev. Lett.* **73** (1994) 373.
- [5] T. Patel and T. Vachaspati, *Structure of electroweak dumbbells*, *Phys. Rev. D* **107** (2023) 093010 [[2302.04886](#)].
- [6] N.S. Manton, *Topology in the Weinberg-Salam Theory*, *Phys. Rev. D* **28** (1983) 2019.
- [7] F.R. Klinkhamer and N.S. Manton, *A Saddle Point Solution in the Weinberg-Salam Theory*, *Phys. Rev. D* **30** (1984) 2212.
- [8] J. Kunz, B. Kleihaus and Y. Brihaye, *Sphalerons at finite mixing angle*, *Phys. Rev. D* **46** (1992) 3587.
- [9] T. Akiba, H. Kikuchi and T. Yanagida, *The Free Energy of the Sphaleron in the Weinberg-Salam Model*, *Phys. Rev. D* **40** (1989) 588.
- [10] B. Acharya, J. Alexandre, P. Benes, B. Bergmann, S. Bertolucci, A. Bevan et al., *Search for magnetic monopoles produced via the schwinger mechanism*, *Nature* **602** (2022) 63.
- [11] D.L.-J. Ho and A. Rajantie, *Electroweak sphaleron in a strong magnetic field*, *Physical Review D* **102** (2020) .
- [12] C.J. Copi, F. Ferrer, T. Vachaspati and A. Achú carro, *Helical magnetic fields from sphaleron decay and baryogenesis*, *Physical Review Letters* **101** (2008) .
- [13] Y.-Z. Chu, J.B. Dent and T. Vachaspati, *Magnetic helicity in sphaleron debris*, *Physical Review D* **83** (2011) .
- [14] PARTICLE DATA GROUP collaboration, *Review of Particle Physics*, *PTEP* **2022** (2022) 083C01.
- [15] T.W. Baumgarte and S.L. Shapiro, *Numerical Relativity: Solving Einstein's Equations on the Computer* (2010).
- [16] T. Vachaspati, *Monopole-Antimonopole Scattering*, *Phys. Rev. D* **93** (2016) 045008 [[1511.05095](#)].
- [17] S.A. Teukolsky, *On the stability of the iterated Crank-Nicholson method in numerical relativity*, *Phys. Rev. D* **61** (2000) 087501 [[gr-qc/9909026](#)].
- [18] M. James, L. Perivolaropoulos and T. Vachaspati, *Detailed stability analysis of electroweak strings*, *Nucl. Phys. B* **395** (1993) 534 [[hep-ph/9212301](#)].
- [19] M. Goodband and M. Hindmarsh, *Instabilities of electroweak strings*, *Phys. Lett. B* **363** (1995) 58 [[hep-ph/9505357](#)].
- [20] J. Urrestilla, A. Achúcarro, J. Borrill and A.R. Liddle, *The Evolution and persistence of dumbbells in electroweak theory*, *JHEP* **08** (2002) 033 [[hep-ph/0106282](#)].
- [21] G. 't Hooft, *Magnetic Monopoles in Unified Gauge Theories*, *Nucl. Phys. B* **79** (1974) 276.
- [22] T. Vachaspati, *Magnetic fields from cosmological phase transitions*, *Phys. Lett. B* **265** (1991) 258.
- [23] T. Vachaspati, *Estimate of the primordial magnetic field helicity*, *Physical Review Letters* **87** (2001) .

A Semilocal Dumbbell simulations

The Z-string has been shown to be stable in the semilocal limit [2], which corresponds to $\sin^2 \theta_w = 1$ and $\beta \equiv m_H^2/m_Z^2 < 1$. As a test of our simulation code, we ran an instance of the dumbbell simulation for the parameters $\sin^2 \theta_w = 0.995$ and $\beta = 0.01$, which lie in the stable regime stated in [2] and studied for a cosmological distribution of dumbbells in [20]. We show several snapshots of the energy density in the xz -plane for the untwisted case ($\gamma = 0$) in Figure 10, and for the twisted case ($\gamma = \pi$) in Figure 11. Unlike the electroweak case, shown in Figures 2 and 3, it can be seen that the Z-string is stable, and the monopole-antimonopole pair move towards each, eventually undergoing annihilation. For the twisted case, we once again observe the formation of an intermediate stable object which eventually decays, and can be seen in Figure 11. The evolution of $\text{Min}[|\Phi|]$ are shown in Figure 12, and the lifetimes are $T_c m_W = 4.9$ and 12.0 , for the untwisted ($\gamma = 0$) and twisted (π) cases, respectively. These lifetimes are much longer than those of the dumbbell in the electroweak case for the same lengths; $T_c m_W = 0.4$ and 7.3 , for twists $\gamma = 0$ and π , respectively.

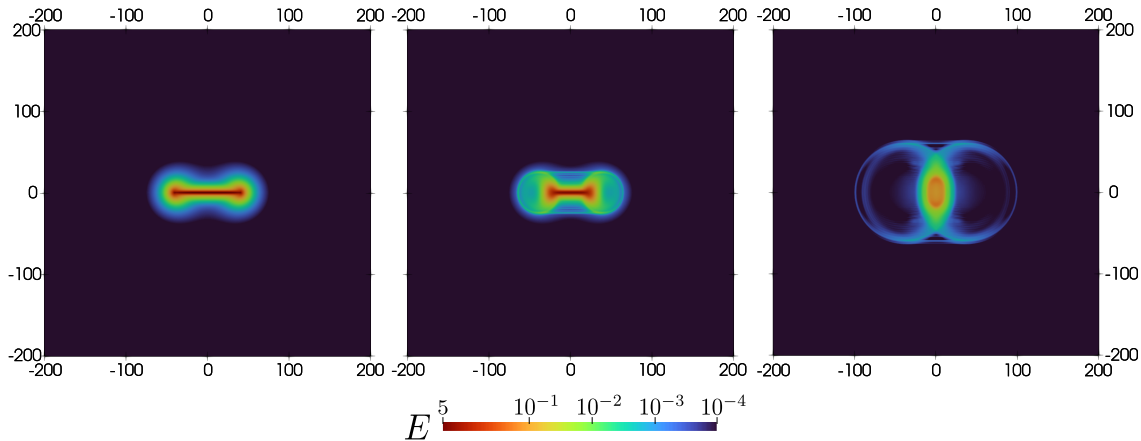


Figure 10: The snapshots of energy density, for dumbbell evolution in the semilocal limit, in xz -plane and twist $\gamma = 0$ are shown here. The left, middle and right panels correspond to times $0dt$, $200dt$ and $500dt$, respectively. The colors represent the energy density and the corresponding values are given by the scale, in units of η^4 . Here, the simulation parameters are $dt = \delta/8$, with $\delta = 0.25\eta^{-1}$, and the initial dumbbell length is $2d = 80\delta$. The horizontal (z) and vertical (x) axis are in lattice units.

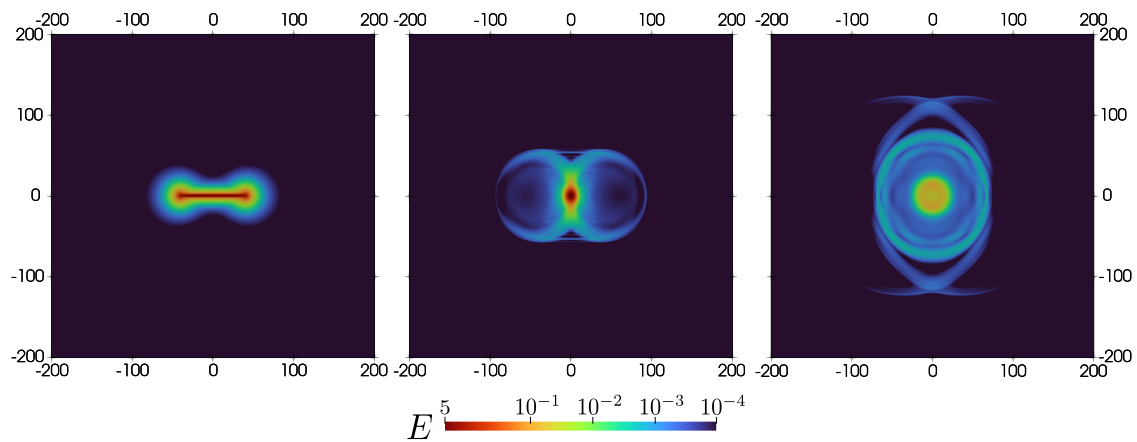


Figure 11: The energy density snapshots, similar to Figure 2, for the twisted case ($\gamma = \pi$) and times $0dt$, $450dt$ and $1000dt$ in the left, middle and right panels, respectively.

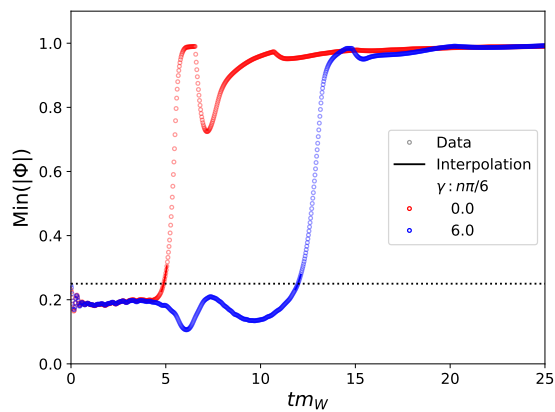


Figure 12: The evolution of $\text{Min}[|\Phi|]$ in the simulation box for twists $\gamma = 0$ (red curve) and π (blue curve). The hollow circles correspond to the data points from the simulation and the solid lines are 4th order polynomial fits around the threshold $\text{Min}[|\Phi|] = 0.25$. We show our threshold choice, $\text{Min}[|\Phi|] = 0.25$, as a dotted horizontal line.